Asian Journal of Pharmaceutical Sciences 17 (2022) 908–923

Available online at www.sciencedirect.com

ScienceDirect

journal homepage: www.elsevier.com/locate/AJPS

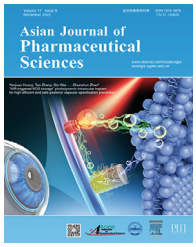

Original Research Paper

Fucoidan-based dual-targeting mesoporous polydopamine for enhanced MRI-guided chemo-photothermal therapy of HCC via P-selectin-mediated drug delivery

Gaofeng Shu[a,b,1], *Lin Shen*[a,1], *Jiayi Ding*[a], *Junchao Yu*[a], *Xiaoxiao Chen*[b], *Xiaoju Guo*[d], *Enqi Qiao*[b], *Yaning Chen*[b], *Chenying Lu*[a,b], *Zhongwei Zhao*[a,b], *Yongzhong Du*[c,*], *Minjiang Chen*[a,b,c,*], *Jiansong Ji*[a,b,*]

[a] *Key Laboratory of Imaging Diagnosis and Minimally Invasive Intervention Research, Institute of Imaging Diagnosis and Minimally Invasive Intervention Research, The Fifth Affiliated Hospital of Wenzhou Medical University, Lishui 323000, China*
[b] *Department of radiology, Lishui Hospital of Zhejiang University, School of Medicine, Lishui 323000, China*
[c] *Institute of Pharmaceutics, College of Pharmaceutical Sciences, Zhejiang University, Hangzhou 310058, China*
[d] *Shaoxing University School of Medcine, Shaoxing 312000, China*

ARTICLE INFO

Article history:
Received 10 February 2022
Revised 6 July 2022
Accepted 14 August 2022
Available online 14 October 2022

Keywords:
Mesoporous polydopamine
Fucoidan
P-selectin target
Platelets bridge
Cancer theranostics

ABSTRACT

The development of novel theranostic agents with outstanding diagnostic and therapeutic performances is still strongly desired in the treatment of hepatocellular carcinoma (HCC). Here, a fucoidan-modified mesoporous polydopamine nanoparticle dual-loaded with gadolinium iron and doxorubicin (FMPDA/Gd^{3+}/DOX) was prepared as an effective theranostic agent for magnetic resonance imaging (MRI)-guided chemo-photothermal therapy of HCC. It was found that FMPDA/Gd^{3+}/DOX had a high photothermal conversion efficiency of 33.4% and excellent T_1–MRI performance with a longitudinal relaxivity (r_1) value of 14.966 $mM^{-1}\cdot s^{-1}$. Moreover, the results suggested that FMPDA/Gd^{3+}/DOX could effectively accumulate into the tumor foci by dual-targeting the tumor-infiltrated platelets and HCC cells, which resulted from the specific interaction between fucoidan and overexpressed p-selectin receptors. The excellent tumor-homing ability and MRI-guided chemo-photothermal therapy therefore endowed FMPDA/Gd^{3+}/DOX with a strongest ability to inhibit tumor growth than the respective single treatment modality. Overall, our study demonstrated that FMPDA/Gd^{3+}/DOX could be applied as a potential nanoplatform for safe and effective cancer theranostics

* Corresponding authors.
E-mail addresses: duyongzhong@zju.edu.cn (Y.Z. Du), minjiangchenv@163.com (M.J. Chen), lschrjjs@163.com (J.S. Ji).
[1] These authors contributed equally to this work.
Peer review under responsibility of Shenyang Pharmaceutical University.

https://doi.org/10.1016/j.ajps.2022.08.004

1. Introduction

Hepatocellular carcinoma (HCC) is still an extremely hard-to-treat disease with poor prognosis, and it is also one of the leading causes for human death worldwide [1]. Currently, the utilization of theranostic agents is considered to be a promising approach for enhanced cancer therapy [2,3]. Due to the simultaneous integration of therapeutic and diagnostic elements in a single nanoplatform, theranostic agents could real-timely provide the knowledges of disease state during the treatment period, thereby largely improving the therapeutic outcomes via imaging-guided therapy [4,5]. In view of practice application, the development of biocompatible theranostic agents with strong bioimaging ability and therapeutic efficacy is highly demanded for the treatment of HCC.

As one of the most commonly used cancer therapies, chemotherapy still suffers from the limited therapeutic effects, and often results in the problem of drug resistance [6]. Recently, many efforts have made on the development of theranostic agents with chemo-photothermal therapy to achieve great synergistic therapeutic effects [7,8]. Photothermal therapy (PTT) is well accepted as a novel noninvasive and harmless cancer treatment technique, which employs the PTT agents to convert adsorbed near-infrared (NIR) light into cytotoxic heat, therefore ablating cancer cells [9–12]. Previous study has evidenced that PTT can enhance the internalization of chemotherapeutic drug into the tumor cells and trigger the drug release from nanoparticles, therefore leading to an enhanced chemotherapy[13]. To data, a variety of inorganic-based PTT agents have shown encouraging results in cancer therapy, such as Au nanomaterials, CuS nanoparticles, and graphene oxide [9,14,15]. However, the potential long-term toxicity of these PTT agents remains a concern that hampers their successful clinical transformation [9,16].

Polydopamine (PDA), as a nature-inspired melanin-like polymer, has recently been recognized as an exciting PTT agent because of its intrinsic biocompatibility, facile functionalization, and high NIR photothermal conversion efficiency [17]. Due to the presence of rich functional groups (ie, catechol, carboxyl and amino groups), PDA has a strong ability to chelate with various metal ions (ie, Fe^{3+}, $Gd^{3+}$and Mn^{2+}), which have been reported to be used as magnetic resonance imaging (MRI) contrast agents for cancer diagnosis [18–20]. Moreover, the presence of abundant aromatic rings in PDA-based nanomaterials endows them a strong ability of directly encapsulating many chemotherapeutic drugs such as doxorubicin (DOX) via π–π stacking and/or hydrophobic interactions [21]. However, the PDA-based nanomedicines are commonly nonporous, which results in a limited drug encapsulation efficiency and loading capacity. In contrast, mesoporous polydopamine (MPDA) offer abundant porous cavities and large surface area for desirably hosting drugs payloads[22]. Apart from efficient drug encapsulation efficacy, MPDA could also provide a significantly higher photothermal conversion efficiency than the nonporous one [23]. Depending on these advantages, the application of MPDA-based theranostic agents might be promising for imaging-guided chemo-photothermal therapy of HCC.

Surface modification is essential for the stability and functionalization of MPDA in practical applications. Fucoidan is a marine polysaccharide that is composed of sulfated ester groups and L-fucopyranose units, which has received considerable attentions in biomedical application due to its potential antitumor, antithrombotic, anticoagulant, and anti-inflammatory activities [24,25]. More importantly, fucoidan is a naturally specific ligand of P-selectin, which is overexpressed on the surface of activated platelets infiltrated in the tumor foci [26,27]. Nanoparticles that hitchhike on the activated platelets have been reported to have a strong ability to track tumor cells via “platelet bridge”. In addition, P-selectin is also upregulated in many types of tumor cells, including HCC [28,29], which may further enhance the tumor-homing capability of P-selectin targeted nanoparticles. Inspire by this, a number of fucoidan-based nanoparticles that can specifically bind with P-selectin on the activated platelets or tumor cells were developed for enhanced cancer diagnosis and cancer therapy [28,30,31]. To our best knowledge, p-selectin targeted PDA-based nanoplatforms for MRI-guided chemo-photothermal combination therapy of cancers have not yet studied.

Herein, a fucoidan-modified MPDA nanoparticle dual-loaded with Gd^{3+} and DOX (FMPDA/Gd^{3+}/DOX) was fabricated as a novel theranostic agent for MRI-guided chemo-photothermal combination therapy of HCC. Gd-based contrast agents (ie, Gd-DTPA and Gd-DOTA) have been widely used in clinical MRI exanimation. Previous study has suggested that Gd could reduce the longitudinal relaxivity (r_1) of the protons the most significantly among all the elements, thus resulting in a significantly enhanced MRI contrast [32]. Fucoidan as a natural ligand of P-selectin could specifically bind to the activated platelets, thereby largely increasing the distribution of FMPDA/Gd^{3+}/DOX in the tumor foci. Besides, the activated platelets could act as a “bridge” to facilitate the internalization of FMPDA/Gd^{3+}/DOX into the cancer cells. Apart from the activated platelet-targeting ability, the fucoidan modification could also endow FMPDA/Gd^{3+}/DOX with a specific ability to bind with the P-selectin upregulated on the cancer cells, therefore further enhancing the tumor-homing capability of FMPDA/Gd^{3+}/DOX. By taking advantage of the dual tumor-targeting ability, FMPDA/Gd^{3+}/DOX could effectively inhibit the tumor growth under NIR irradiation via the chemo-photothermal combination therapy. In addition, due to the chelation of Gd^{3+}, FMPDA/Gd^{3+}/DOX had a satisfactory MRI-T_1 performance that could track the tumor progression. Overall, the present work reveals that the resultant FMPDA/Gd^{3+}/DOX could be applied as a pleasurable theranostic agent for enhanced imaging-guided chemo-photothermal combination therapy of HCC.

2. Materials and methods

2.1. Materials

Dopamine hydrochloride, gadolinium (III) chloride ($GdCl_3$), ammonia ($NH_3{\cdot}H_2O$, 25%–28%), DOX, cysteamine, chloroacetic

acid, sodium citrate, citric acid, and dextrose were purchased from Aladdin Bio-Chem Technology Co., Ltd. (Shanghai, China). mPEG-SH (Mw=5000) was purchased from Seebio Biotechnology Co., Ltd. (Shanghai, China). Fucoidan, Pluronic 123, Pluronic F127, tetrazolium (MTT), indocyanine green dye (ICG), and 1,3,5-trimethylbenzene (TMB) were purchased from Sigma Chemical Co. (St. Louis, MO). Anti-CD41 antibody was purchased from Abcam, Inc. (Cambridge, MA, USA). Anti-CD62P (P-selectin) antibody was purchased from Boster Co., Ltd. (Wuhan, China). All other chemicals were of analytical grade.

2.2. Cell line and animals

Human hepatoma LM3 cells were purchased from American Type Culture Collection (ATCC, Manassas, VA, USA). The cells were cultured in Dulbecco's modified eagle medium (DMEM, Gibco BRL, USA) supplemented with 10% of fetal bovine serum (FBS, Gibco BRL, USA) and penicillin/streptomycin (100 U/ml, 100 U/ml) at 37 °C with a humidified atmosphere of 5% CO_2.

Balb/c nude male mice (4–5 weeks, ~16 g) were purchased from Shanghai Silaike Laboratory Animal Co., Ltd. All animal procedures were performed in accordance with the Guidelines for Care and Use of Laboratory Animals of Zhejiang University and approved by the Animal Ethics Committee of Zhejiang University. The tumor-bearing animal models were built by subcutaneously injecting LM3 cells into the axillary of Balb/c nude mice.

2.3. Synthesis of carboxyl fucoidan

The synthesis of carboxyl fucoidan (FU-COOH) was carried out according to a method reported in a previous study [33]. In brief, 1 g of fucoidan (FU) and 0.8 g NaOH were dissolved within 20 ml distilled water, followed by adding 1 g chloroacetic acid under magnetic stirring. The resultant mixture was then heated to 70 °C in a water bath, which was thereafter allowed to react for 3 h. After reaction, the mixture was added with 150 ml methanol to precipitate the product. The precipitates were re-dissolved within 10 ml distilled water, which was then purified by dialyzing against distilled water for 3 d. Finally, FU-COOH was obtained by lyophilization.

2.4. Synthesis of thiolated fucoidan

The synthesis of thiolated fucoidan (FU-SH) was performed by a previous protocol with a slight modification [34]. Briefly, 500 mg FU-COOH was dissolved within 20 ml distilled water, followed by adding 1197.5 mg EDC and 575.0 mg NHS to activate the carboxyl groups in FU-COOH. After 60 min incubation, the activated FU-COOH was reacted with 710 mg cysteamine for 24 h at ambient temperature. The product was then dialyzed against distilled water for 3 d, and then lyophilized to obtain FU-SH powder. The obtained FU-SH was characterized by Proton nuclear magnetic resonance (^1H NMR, AC-80, Bruker Bios pin. Germany) and Fourier-transform infrared spectroscopy (FTIR, VECTOR22, Bruker), respectively.

2.5. Preparation of fucoidan-modified MPDA nanoparticles

Firstly, MPDA was fabricated according to a published method by using F127 and P123 as templates [35]. P123 and F127 are two similar triblock copolymers from Pluronic family with hydrophilic chains of different lengths, which are often used as soft templates to prepare MPDA. Previous study has suggested that the pore diameter and structures of MPDA could be controlled by finely tuning the mass ratio of P123 to F127 in the reaction system [35]. In this study, F127 (75 mg), P123 (30 mg), and dopamine hydrochloride (150 mg) were dissolved within 10 ml ethanol solution (40%, v/v), followed by adding 0.4 ml TMB. The mixture was then sonicated to homogeneous emulsions by a sonicator. After that, the resultant mixture was quickly introduced with 0.4 ml $NH_3{\cdot}H_2O$ (25%–28%), which was then allowed to react for 4 h at ambient temperature under vigorously stirring. The products of MPDA was then collected by centrifugation, followed by washing with water and ethanol for 3 times, respectively. Fucoidan-modified MPDA (FMPDA) was prepared by mixing MPDA (1 mg/l) and FU-SH (10 mg/l) under magnetic stirring. After 24 h, the excess FU-SH was removed by centrifugation and washing with water 3 times. In another experiment of this study, PEGylated MPDA as a control group was synthesized by the similar procedure, where FU-SH was replaced by mPEG-SH.

2.6. Preparation of Gd^{3+}-chelated FMPDA

FMPDA chelated with Gd^{3+} (FMPDA/Gd^{3+}) was prepared by adding $GdCl_3$ solution (0.2 mg/ml) into the same volume of FMPDA dispersions (1 mg/ml) under stirring. After 8 h, the unchelated $Gd^{3+}$was removed by centrifugation and washing with water 3 times. The concentration of Gd in the obtained products was measured through an inductively coupled plasma-mass spectrometry (ICP-MS) method. In another experiment of this study, PEGylated MPDA chelated with Gd^{3+} (namely MPDA/Gd^{3+}) was prepared using the same method.

2.7. Characterization of the samples

The particle size and size distribution of the samples were evaluated by a dynamic light scattering equipment (DLS, litesizer 500, Anton-Paar, Austria). The morphologies of the samples were characterized by a transmission electronic microscopy (TEM; JEM-1200EX, JEOL, Japan). Energy-dispersive X-ray (EDX) analysis was performed on a scanning electronic microscopy (SEM; Hitachi SU-8010, Tokyo, Japan). The UV–vis absorption spectra of the samples were measured using a UV-2600 spectrophotometer (UV-2600, Shimadzu, Japan). The Gd concentrations were analyzed by an Agilent Technologies 7800 ICP-MS (Santa Clara, CA, USA). The mesoporous structure of samples was also further analyzed by Brunauer-Emmett-Teller (BET) method.

2.8. DOX encapsulation and release performance

DOX-loaded FMPDA/Gd^{3+} nanoparticles (FMPDA/Gd^{3+}/DOX) were prepared by simply mixing FMPDA/Gd^{3+} (1 mg/ml,

2 ml) with DOX (0.4 mg/ml, 2 ml) in PBS solution (pH = 8) for 36 h in dark condition. Then, the solution was centrifugated and washed with distilled water for 3 times to remove the unabsorbed DOX. The DOX concentration in the collected supernatants was quantified by a UV–vis spectrophotometer, which was then used for calculating the encapsulation efficiency (EE) and drug loading (DL) of DOX in FMPDA/Gd^{3+}/DOX.

The laser-triggered drug release performance of FMPDA/Gd^{3+}/DOX was carried out by NIR irradiation at a wavelength of 808 nm. In brief, a known amount of FMPDA/Gd^{3+}/DOX were dispersed into PBS solutions with a pH value of 7.4 and 5.0, respectively. At the selected time interval, FMPDA/Gd^{3+}/DOX solutions were treated with or without NIR irradiation (2 W/cm^2) for 5 min. The amount of DOX released from the FMPDA/Gd^{3+}/DOX were determined using UV–vis spectroscopy.

2.9. *In vitro photothermal performance*

To evaluate the photothermal ability FMPDA/Gd^{3+}/DOX, 1 ml sample were placed in a cuvette with different MPDA concentrations, which were then treated with NIR irradiation for 10 min (2 W/cm^2). The changes of solution temperature at a selected time interval were recorded by a digital thermometer. The photothermal stability was examined by detecting the temperature profiles of FMPDA/Gd^{3+}/DOX solutions (0.5 mg/ml), which were irradiated by 4 cycles of NIR light at a power density of 2 W/cm^2. Besides, the photothermal conversion efficiency of FMPDA/Gd^{3+}/DOX was evaluated by Roper's method [36].

2.10. *In vitro MRI*

The T_1-weighted images and T_1 relaxation time of FMPDA/Gd^{3+}/DOX were measured by a 3.0 T MRI Scanner (Philips Achieva 3.0 T TX). Then, the relaxivity value (r_1) of FMPDA/Gd^{3+}/DOX was calculated by fitting $1/T_1$ relaxation time (s^{-1}) *vs* Gd concentration curve, and Gd-DOTA was applied as a control.

2.11. *In vitro binding test of activated platelets and FMPDA/Gd^{3+}/DOX*

The platelets were firstly isolated from the whole blood of Balb/c nude mice according to a previously reported procedure [37]. Briefly, the whole blood was collected into 1.0 ml citrate buffer (pH=7.4) containing sodium citrate (90 mM), NaH_2PO_4 (16 mM), citric acid (16 mM), and dextrose (142 mM). Next, the upper platelet-rich plasma (PRP) was collected by centrifuging the whole blood at ambient temperature (150 g, 15 min). Subsequently, the PRP was centrifuged at 800 g for 15 min to get platelet pellets. The collected platelet pellet was then carefully suspended in PBS solution (pH=7.4) for the following experiments.

In vitro binding ability of activated platelets and FMPDA/Gd^{3+}/DOX was studied using a confocal laser scanning microscope (CLSM). Firstly, the platelets were activated by incubating them with thrombin (0.5 U/ml) at 37 °C for 30 min. Then, the activated and non-activated platelets were treated with FMPDA/Gd^{3+}/DOX or MPDA/Gd^{3+}/DOX (as control) at 37 °C for 30 min. To remove the unbonded nanoparticles, the platelets were centrifugated at 800 g for 20 min. Then, the obtained platelet pellets were re-dispersed in PBS, followed by photographing the fluorescent images under CLSM. In addition, the mean fluorescence intensity of DOX in normal platelets and thrombin-activated platelets was quantified by flow cytometry (BD FACSVia, BD Biosciences). In another experiment of this study, the activated platelets were pretreated with anti-CD62P antibody (5 μg/ml) for 30 min before the incubation of FMPDA/Gd^{3+}/DOX.

2.12. *Cellular uptake behaviors*

The cellular uptake study of FMPDA/Gd^{3+}/DOX was also performed by CLSM method. In brief, LM3 cells were seeded in 24-well plates for incubating 24 h. After that, the cells were incubated with FMPDA/Gd^{3+}/DOX or MPDA/Gd^{3+}/DOX at a dose of DOX 5 μg/ml for 1 or 6 h, respectively. The cells were then washed with PBS, stained with DAPI, and subsequently subjected to fluorescence imaging. For the competitive analysis, the cells were pretreated with anti-CD62P antibody (5 μg/ml) for 30 min before adding FMPDA/Gd^{3+}/DOX. To study the effect of NIR irradiation on the cellular uptake behavior, the cells were irradiated by an 808 nm laser at a power density of 2 W/cm^2 for 5 min at 5 h of post-incubation with FMPDA/Gd^{3+}/DOX, followed by incubation for another 1 h.

In order to evaluate whether the presence of platelets could influence the cellular uptake behaviors, LM3 cells were pre-incubated with the activated platelets for 30 min, followed by incubating with FMPDA/Gd^{3+}/DOX and MPDA/Gd^{3+}/DOX for 1 h. The LM3 cells were then stained with DAPI and observed by CLSM. In addition, the mean fluorescence intensity of DOX in each sample was quantified by flow cytometry.

2.13. *In vitro cytotoxicity test*

The cytotoxicity of FMPDA/Gd^{3+}/DOX against LM3 cells were analyzed by MTT assays. In brief, 0.2 ml LM3 cells were seeded into 96-well plates at a density of 1×10^4 cells per well. After 24 h of incubation, the cells were treated with FMPDA/Gd^{3+}/DOX at a different DOX dose for 48 h. Then, the cells in each well were added with 20 μl MTT solution (5 mg/ml), which were allowed to incubate for another 4 h. After removing the medium, the purple formazan product was dissolved by DMSO for 15 min. Then, the absorbance of each sample at 570 nm was measured by an automatic microplate reader. The cells without any treatment were used as control groups. The cell viability was calculated by the following formula: Cell viability = $Abs_{(test\ cells)}/Abs_{(control\ cells)}$. Moreover, the cell viability of MPDA/Gd^{3+}/DOX and free DOX were also detected using the same method.

The chem-photothermal combination therapy of FMPDA/Gd^{3+}/DOX on LM3 cells was also evaluated. In brief, LM3 cells in 96-well plates were treated with different concentrations of FMPDA/Gd^{3+}/DOX and FMPDA/Gd^{3+} for 12 h. The corresponding well was irradiated with NIR light at a power density of 2 W/cm^2 for 5 min, which was then incubated for another 2 h. The cells without NIR irradiation or drug were used as controls. The corresponding cell

viability was determined by MTT assay as described above. In another experiment of this study, the cells after treatment (MPDA=80 μg/ml) were rinsed and stained with calcein-AM for fluorescence microscopy observation.

2.14. *In vivo distribution*

In vivo distribution of FMPDA/Gd^{3+}/DOX was investigated by using a subcutaneous tumor-bearing mice model. As a replacement of DOX, an infrared dye ICG was used to label FMPDA/Gd^{3+}(abbreviated as FMPDA/Gd^{3+}/ICG) before study. The tumor-bearing mice were intravenously injected with FMPDA/Gd^{3+}/ICG or MPDA/Gd^{3+}/ICG at the same ICG dosage. At a preselected time, the mice were imaged by Maestro EX In Vivo Imaging System (CRI Inc., Woburn, MA). The fluorescent signals of tumor tissues and major organs (heart, liver, spleen, lung and kidney) harvested at 24 h were detected with the same parameters. Moreover, the harvested tumor tissues were subjected to frozen slices, stained with DAPI, P-selectin or CD41 for CLSM observation.

2.15. *In vivo MRI and infrared thermal imaging*

For *in vivo* MRI, the tumor-bearing mice were intravenously administrated with FMPDA/Gd^{3+}/DOX or MPDA/Gd^{3+}/DOX at a dosage of MPDA 12 mg/kg. The subcutaneous tumors were observed using a 3.0T MRI scanner at predetermined time points after injection. The T_1-weighted MRI parameters were shown as follows: TR, 290 ms, TE, 15 ms, FOV, 70 × 70, matrix size, 304 × 201, slice thickness, 2.0 mm.

For *in vivo* infrared thermal imaging, the tumor-bearing mice were intravenously administrated with FMPDA/Gd^{3+}/DOX or MPDA/Gd^{3+}/DOX at a dosage of MPDA 12 mg/kg. The mice treated with PBS were used as a control group. After 24 h, the tumor site was subjected to NIR irradiation (808 nm) at a power density of 2 W/cm^2 for 5 min. The infrared thermal images of mice were then obtained by an infrared camera thermographic system (FLTR, USA).

2.16. *In vivo anticancer efficacy and toxicity evaluation*

The mice subcutaneously bearing LM3 with a tumor volume of approximately 100 mm^3 were randomly divided into 7 groups (n = 5 for each groups). The mice in each group were treated with PBS, PBS+NIR, free DOX, FMPDA/Gd^{3+}+NIR, MPDA/Gd^{3+}/DOX, FMPDA/Gd^{3+}/DOX, and FMPDA/Gd^{3+}/DOX+NIR (MPDA=12 mg/kg, and DOX= 4.2 mg/kg), respectively. The mice were intravenously injected with the above preparations for total 2 times at Day 1 and 3, respectively. The mice with photothermal treatment were subjected to NIR irradiation at 2 W/cm^2 for 5 min after 24 h of injection. The tumor volume and body weight were recorded every 2 d during treatment. The tumor volume was calculated by the following formula: V=length × $width^2$/2. At the last treatment day, the mice were sacrificed, and their blood, tumor tissues and major organs (heart, liver, spleen, lung and kidney) were harvested. The levels of aspartate transaminase (AST), alanine aminotransferase (ALT), creatinine (CRE) and urea nitrogen (BUN) in the blood serum were measured. The major organs were stained with H&E, and the tumor tissues were stained with H&E, TUNEL and Ki-67, respectively.

2.17. *Western blotting analysis*

The expression levels of P-selectin on normal platelets, thrombin-activated platelets and LM3 cells were evaluated by western blotting analysis. The platelets and LM3 cells were homogenized and lysed in ice-cold RIPA lysis buffer. The concentration of protein in each sample was then quantified by a bicinchoninic acid assay (Beyotime Biotechnology, Shanghai, China). The protein with an equivalent amount was separated by SDS-PAGE, following by transferring to a PVDF membrane (0.22 μm, Milipore). After blocked for 90 min in blocking buffer at room temperature, the membranes were incubated with the primary antibody anti-(CD62P) overnight at 4 °C. Afterwards, the membranes were incubated with an appropriate secondary antibody for 60 min at room temperature. The target bonds were visualized by an ECL chemiluminescence kit, and GAPDH was used as the control protein.

2.18. *Statistical analysis*

All values were expressed as means ± standard deviation (SD). Statistical significance was performed using a two-tailed Student's *t*-test. P <0.05 was considered statistically significant.

3. Results and discussion

3.1. *Synthesis and characterization of FMPDA/Gd^{3+}*

The synthetic route of FMPDA/Gd^{3+} was illustrated in Fig. 1A. Firstly, cysteamine-fucoidan conjugate (FU-SH) as a stabilizer for MPDA was prepared according to the procedure displayed in Fig. S1A. After FU-SH synthesis, ^1H NMR and FTIR measurements were performed to confirm whether cysteamine was successfully conjugated on fucoidan or not. As shown in Fig. S1B, the ^1H NMR spectrum of FU-SH had newly formed peaks at approximately 2.70 and 3.10 ppm relative to that of fucoidan, which was belonged to the characteristic peaks of cysteamine (2.70 ppm was corresponding to the CH_2 groups connecting the amine group, whereas 3.10 ppm was corresponding to the CH_2 groups connecting the thiolated group). In addition, the FTIR spectrum of FU-SH not only showed the characteristic bands of fucoidan at 1258 cm^{-1} (stretch vibration of S = O bond) and 844 cm^{-1} (stretch vibration of C–O-S bond), but also exhibited a newly weak band at 2510 cm^{-1}, which was belonged to the stretch vibration of -SH group (Fig. S1C). Apparently, ^1H NMR and FTIR examinations both verified that FU-SH was successfully synthesized in our study.

Subsequently, MPDA was prepared by a simple emulsion-induced interfacial anisotropic assembly approach, in which the assembly of PDA seeds in the F127/P123-stabilized TMB emulsion droplet templates could lead to mesoporous structures [35]. As shown in Fig. 1B, the prepared MPDA exhibited mesoporous structure and spherical morphologies,

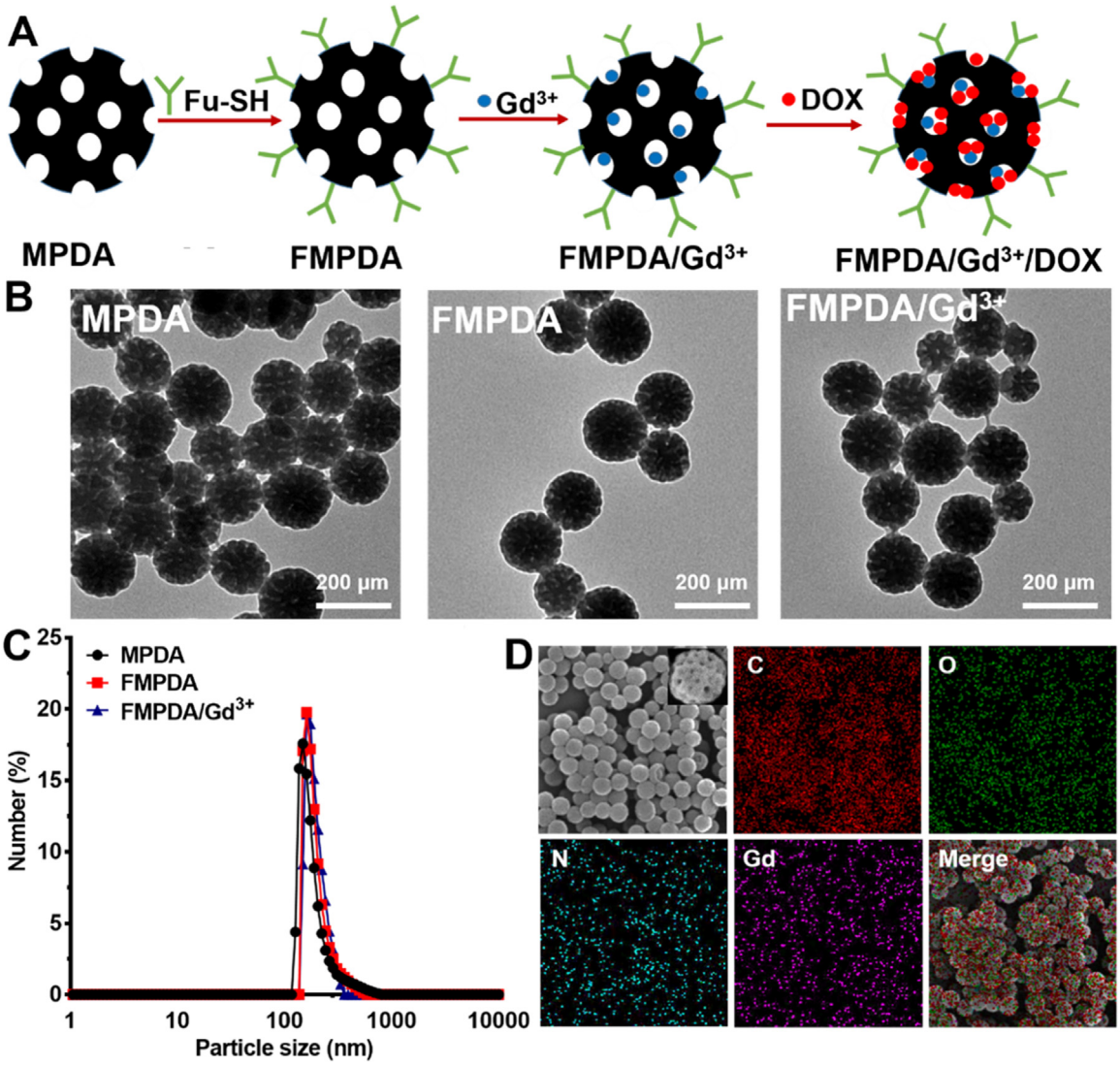

Fig. 1 – Preparation and characterization of FMPDA/Gd^{3+}/DOX. (A) Schematic illustration of FMPDA/Gd^{3+}/DOX formulation. TEM images (B) and size distribution (C) of MPDA, FMDA, and FMPDA/Gd^{3+}. (D) FESEM images and the corresponding EDX elemental mapping images of FMPDA/Gd^{3+}.

with nearly uniform diameters of approximately 150 nm. In addition, it was found that the average particle diameter of MPDA measured through DLS was 165 ± 9 nm (Fig. 1C), which was consistent with the TEM result.

MPDA was then functionated with fucoidan by simply mixing FU-SH and MPDA suspensions under an alkaline condition. As shown in Fig. S2A, the FTIR spectrum of FMPDA exhibited a newly formed band at 1258 cm^{-1} (stretch vibration of S=O bond in fucoidan), which suggested that fucoidan was successfully grafted onto MPDA. Moreover, we found that FMPDA was stable without evidence of particle precipitations during storage in PBS overnight, whereas the MPDA without surface modification was quite unstable under the same condition (Fig. S2B), which further verified that MPDA was successfully modified by fucoidan. The conjugation of FU-SH onto MPDA was due to that the catechol/quinine groups of MPDA could easily react with the -SH groups of FU-SH via Michael addition or Schiff base reaction under an alkaline environment [38]. The particle size of FMPDA (172 ± 6 nm) was slightly larger than MPDA (Fig. 1C), which was possibly due to the surface modification of fucoidan. However, the morphology of MPDA had little impact by the surface modification of fucoidan (Fig. 1B).

It is well documented that PDA-based materials have a variety of functional groups (*e.g.*, carboxyl, amino, and catechol groups) that could directly complex with different metal ions, including Cu^{2+}, Fe^{3+}, Mn^{2+} and Gd^{3+} ions [39]. Thus, the fabrication of FMPDA/Gd^{3+}were performed by simply mixing $GdCl_3$ with FMPDA/Gd^{3+} nanosuspensions at ambient temperature. The elemental composition of FMPDA/Gd^{3+} was determined by FESEM-EDS analysis, which showed a uniform distribution of C, N, O and Gd elements in FMPDA/Gd^{3+} (Fig. 1D). This result suggested that Gd^{3+} was successfully chelated within FMPDA/Gd^{3+}. Moreover, FESEM-EDS analysis showed that the content of Gd^{3+} in FMPDA/Gd^{3+} was 3.37% (Fig. S2C), which was in consistent with the ICP-

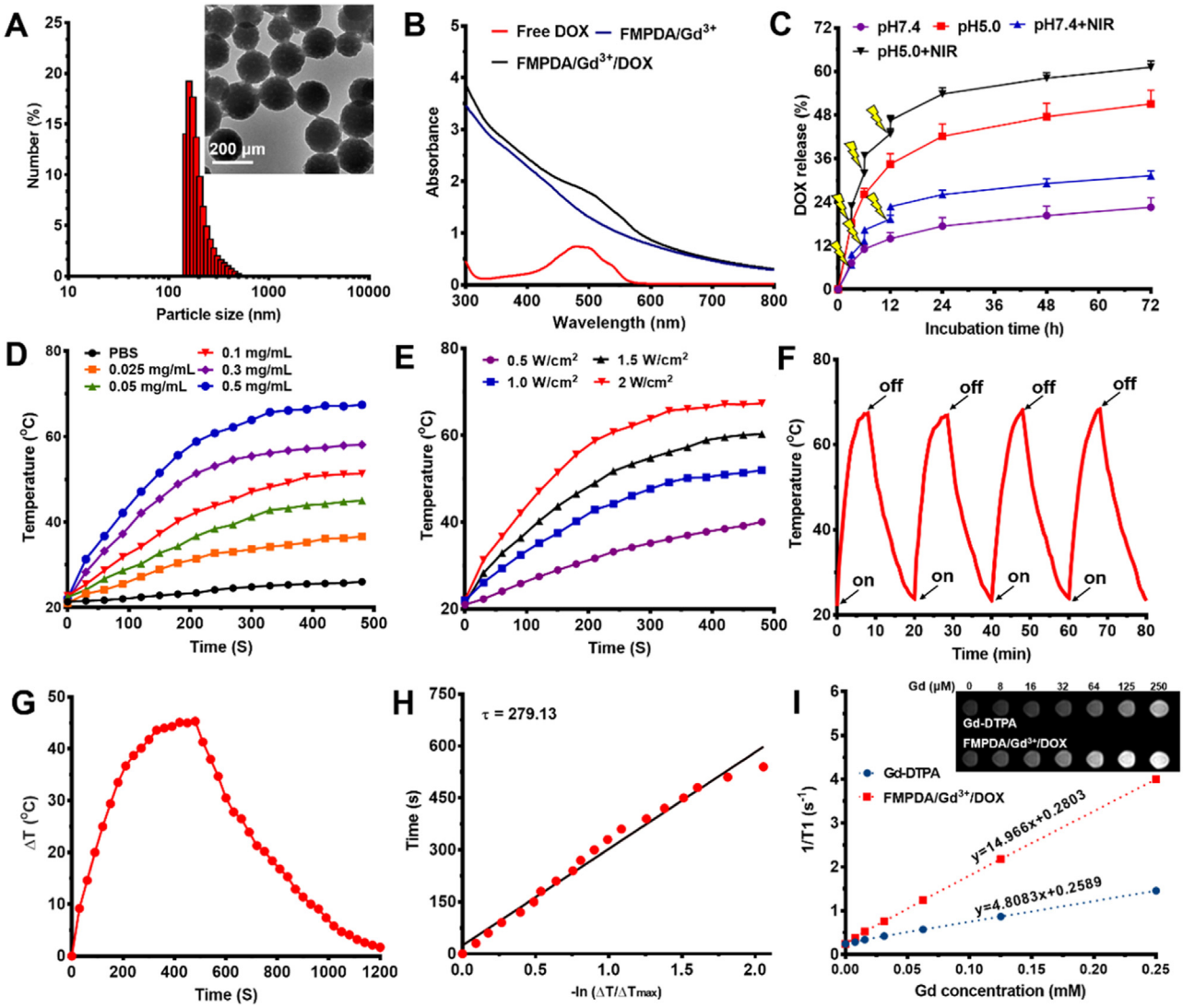

Fig. 2 – Characterization of FMPDA/Gd^{3+}/DOX. (A) TEM image and size distribution of FMPDA/Gd^{3+}/DOX. (B) UV–vis absorption spectra of free DOX, FMPDA/Gd^{3+} and FMPDA/Gd^{3+}/DOX. (C) *In vitro* DOX release behavior of FMPDA/Gd^{3+}/DOX. (D) Temperature elevation of FMPDA/Gd^{3+}/DOX as a function of MPDA concentration (2 W/cm^2). (E) Temperature elevation of FMPDA/Gd^{3+}/DOX as a function of NIR powder intensity (MPDA=0.5 mg/mL). (F) Photostability of FMPDA/Gd^{3+}/DOX under 4 cycles of photothermal heating and natural cooling (MPDA=0.5 mg/ml, 2 W/cm^2). (G) Photothermal effect of the aqueous dispersion of FMPDA/Gd^{3+}/DOX (0.5 mg/ml) under NIR laser irradiation (2 W/cm^2) for 10 min. (H) Linear time date *versus* -lnθ obtained from the cooling period. (I) T_1 relaxation rate of FMPDA/Gd^{3+}/DOX and Gd-DTPA, and the insert images were T_1-weighted MR images of FMPDA/Gd^{3+}/DOX and Gd-DTPA.

MS data (~2.97%). On the other hand, it was found that the Gd^{3+} chelation had no significant impact on the particle size and morphology of FMPDA (Fig. 1B and 1C). The mesoporous structure of FMPDA/Gd^{3+} was also further analyzed using BET method. As shown in Fig. S3, the N2 adsorption–desorption isotherms of MPDA and FMPDA/Gd^{3+} both exhibited typical type-IV hysteresis, suggesting the presence of mesopores. The resulting MPDA and FMPDA/Gd^{3+} showed BET surface areas of 16.38 and 15.84 m^2/g, respectively. This result suggested that the Gd^{3+} chelation and fucoidan modification had slightly impact on the surface area and MPDA.

3.2. *DOX loading and release properties*

Due to the excellent ability to kill cancer cells, DOX was selected as a model drug to investigate the performance of FMPDA/Gd^{3+} as a drug carrier. In our study, the preparation of DOX-loaded FMPDA/Gd^{3+} (FMPDA/Gd^{3+}/DOX) was performed by simply mixing DOX and FMPDA/Gd^{3+} in PBS solution. The as-prepared FMPDA/Gd^{3+}/DOX had spherical particles with an average size of 184 ± 5 nm (Fig. 2A). As displayed in Fig. 2B, a typical adsorption peak of DOX at around 480 nm was appeared in the spectrum of FMPDA/Gd^{3+}/DOX

relative to that of FMPDA/Gd^{3+}, demonstrating the successful encapsulation of DOX within FMDA/Gd^{3+}/DOX. In addition, UV–Vis measurement revealed that EE and DL of DOX in FMPDA/Gd^{3+}/DOX was about 88% and 27%, respectively. The remarkable ability of FMPDA/Gd^{3+} to encapsulate DOX was not surprised, because DOX had aromatic structures that could be effectively loaded within MPDA via their π-π stacking and/or hydrophobic interactions [22]. The stability of FMPDA/Gd^{3+}/DOX in PBS and PBS+10% FBS (pH 7.4, 25 °C) was evaluated. It was found that the average particle size of FMPDA/Gd^{3+}/DOX was not significantly increased during 7 d of storage in PBS and PBS+10%FBS (Fig. S4). This result suggested that FMPDA/Gd^{3+}/DOX had an excellent stability in physiological environment.

The drug release properties of FMPDA/Gd^{3+}/DOX were firstly examined in PBS solutions with different pH values. As exhibited in Fig. 2C, only 22.6% of DOX was released from FMPDA/Gd^{3+}/DOX at pH 7.4 within 72 h. In comparison, 51.1% of DOX was released at pH 5.0 within the same time, which was possibly due to the enhanced solubility of protonated DOX at a lower pH. The pH-responsive drug release behavior suggested that FMPDA/Gd^{3+}/DOX was suitable for effectively delivering DOX into the tumor sites without premature drug leakage during blood circulation. Subsequently, the effect of NIR irradiation on the drug release profiles of FMPDA/Gd^{3+}/DOX was investigated. It was observed that the DOX release rate was significantly increased when FMPDA/Gd^{3+}/DOX were exposed to NIR irradiation. It should be also noted that the enhanced DOX release rate upon NIR irradiation is more pronounced at pH 5.0. The NIR-responsive drug release behavior could be attributed to that MPDA converted the NIR light to heat energy, thereby resulting in the dissociation of DOX from MPDA [40]. The dual pH/NIR-responsive DOX release properties made FMPDA/Gd^{3+}/DOX promising for effective drug delivery and controlled chemotherapy, which was extremely beneficial for cancer treatment.

3.3. *In vitro photothermal performance*

It is widely accepted that PDA-based materials can generate heat by converting the adsorbed NIR light, thereby performing as excellent PTT agents for cancer therapy [41]. To investigate the photothermal performance of FMPDA/Gd^{3+}/DOX, the temperature changes of FMPDA/Gd^{3+}/DOX nanosuspensions under 808 nm NIR irradiation were recorded by a digital thermometer. As observed in Fig. 2D, FMPDA/Gd^{3+}/DOX exhibited a concentration-dependent photothermal heating effect. After 10 min of NIR irradiation (2 W/cm^2), the temperature of FMPDA/Gd^{3+}/DOX nanosuspensions could be increased by ~45 °C at a MPDA concentration of 0.5 mg/ml, while the distilled water was only increased by ~5 °C. Besides, the temperature changes of FMPDA/Gd^{3+}/DOX under NIR irradiation (2 W/cm^2) for different time was also characterized by IR thermal imaging (Fig. S5), and the result was consistent with the data obtained using a digital thermometer. We also found that the photothermal performance of FMPDA/Gd^{3+}/DOX and MPDA/Gd^{3+}/DOX was quite similar (Fig. S6), suggesting that the modification of fucoidan had no impact on the photothermal capacity of MPDA. In addition, the photothermal effect of FMPDA/Gd^{3+}/DOX varied with the power density of NIR irradiation. As shown in Fig. 2E, the temperature of FMPDA/Gd^{3+}/DOX dispersion (MPDA=0.5 mg/ml) increased more quickly under NIR irradiation with a higher power density, reflecting a laser power-dependent manner. Through 4 cycles of irradiation/cooling tests, FMPDA/Gd^{3+}/DOX exhibited a high photostability without photodegradation occurrence (Fig. 2F). According to Fig. 2G and 2H, the photothermal conversion efficiency of FMPDA/Gd^{3+}/DOX was calculated to be 33.4%, which was in compliance with the other MPDA-based photothermal agents reported in previous studies [40,42]. These obtained results verified that FMPDA/Gd^{3+}/DOX could be a promising agent for PTT because of its excellent photothermal effects and photostability.

3.4. *In vitro MRI*

To evaluate the feasibility of FMPDA/Gd^{3+}/DOX as a platform for MRI, *in vitro* T_1-weighted MR imaging was performed by a 3.0 T MRI scanner. As shown in Fig. 2I, the T_1-weighted images of FMPDA/Gd^{3+}/DOX displayed a signal enhancement along with the increase of Gd concentration, therefore leading to a brighter image. Moreover, the T_1 relaxivity value (r_1) of FMPDA/Gd^{3+}/DOX was determined by measuring the longitudinal proton relaxation rate ($1/T_1$) as a function of Gd concentration. According to Fig. 2I, the r_1 value of FMPDA/Gd^{3+}/DOX was calculated to be 14.966 $mM^{-1}\cdot s^{-1}$, which was approximately 3-fold higher than that of the commercial Gd-DTPA (4.808 $mM^{-1}\cdot s^{-1}$). This result indicated that the MRI performance of free Gd could be significantly amplified by encapsulation it within MPDA, and the reason was closely associated with the additive effect of all the Gd^{3+} paramagnetic centers and the reduction of molecular tumbling rates [43,44].

3.5. *In vitro activated platelets binding evaluation*

To evaluate the targeting ability of FMPDA/Gd^{3+}/DOX towards activated platelets, platelets was isolated from the whole blood of mice and then activated by thrombin. Western blotting analysis confirmed that P-selectin was overexpressed on thrombin-activated platelets, but not on normal platelets (Fig. S7). Subsequently, the thrombin-activated and non-activated platelets were incubated with FMPDA/Gd^{3+}/DOX at 37 °C for 30 min before CLSM measurements. The platelets treated with MPDA/Gd^{3+}/DOX were served as control groups. As shown in Fig. 3A, after incubation with FMPDA/Gd^{3+}/DOX, the activated platelets exhibited a considerably stronger DOX fluorescence signal (red color) than that of the non-activated platelets. In contrast, both of the activated and non-activated platelets showed quite weak fluorescence intensities after incubating with MPDA/Gd^{3+}/DOX. These results indicated that FMPDA/Gd^{3+}/DOX could bind onto the activated platelets with a high affinity. In order to verify the specific binding of FMPDA/Gd^{3+}/DOX onto the activated platelets was mediated by fucoidan and P-selectin interactions, the activated platelets were pretreated with P-selectin antibody before incubation with FMPDA/Gd^{3+}/DOX. Consequently, the red fluorescence intensity of DOX in activated platelets was sharply weakened

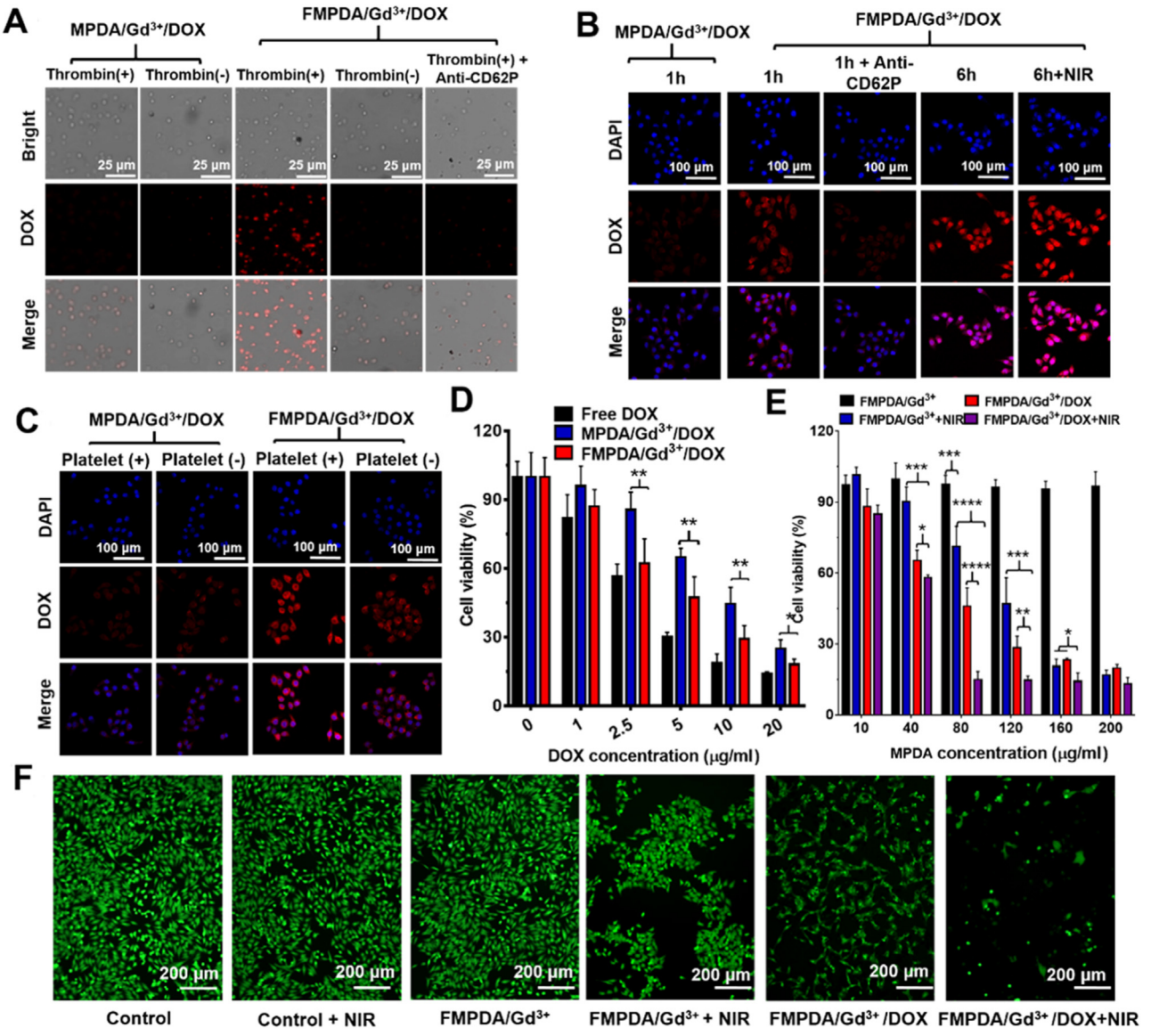

Fig. 3 – *In vitro* targeting ability and anti-cancer evaluation. (A) CLSM images of thrombin-activated and non-activated platelets treated with FMPDA/Gd^{3+}/DOX or MPDA/Gd^{3+}/DOX for 30 min. In the case of competitive assay, thrombin-activated platelets were pretreated with Anti-CD62P antibody for 30 min. (B) CLSM images of LM3 cells treated with FMPDA/Gd^{3+}/DOX or MPDA/Gd^{3+}/DOX for 1 h or 6 h, respectively. In the case of competitive assay, LM3 cells were pretreated with Anti-CD62P antibody for 30 min. (C) CLSM images of LM3 cells after incubating with FMPDA/Gd^{3+}/DOX or MPDA/Gd^{3+}/DOX for 1 h, in the presence of absence of the activated platelets. (D) The cell viability of LM3 cells treated with free DOX, MPDA/Gd^{3+}/DOX or FMPDA/Gd^{3+}/DOX at different DOX dose for 48 h. (E) The cell viability of LM3 cells treated with different concentrations of FMPDA/Gd^{3+} or FMPDA/Gd^{3+}/DOX for 12 h, followed by the treatment with or without NIR irradiation (2 W/cm^2, 5 min) and then incubation for another 2 h. (F) The fluorescent images of survival LM3 cells in different treatment groups (MPDA= 80 μg/ml). (*$P < 0.05$, ** $P < 0.01$, *** $P < 0.001$, **** $P < 0.0001$, $n = 5$).

due to the pretreatment of P-selectin antibody (Fig. 3A), which confirmed that FMPDA/Gd^{3+}/DOX could specifically interact with P-selectin on thrombin-activated platelets. The targeting ability of FMPDA/Gd^{3+}/DOX toward activated platelets was further confirmed by flow cytometry (Fig. S8A and S8B), which was consistent with the results obtained from CLSM examination.

3.6. *In vitro cellular uptake*

In vitro cellular uptake was firstly performed to evaluate whether FMPDA/Gd^{3+}/DOX could target the tumor cells or not. As shown in Fig. 3B, LM3 cells treated with FMPDA/Gd^{3+}/DOX for 1 h had a considerably stronger fluorescence signal (red color) than that of MPDA/Gd^{3+}/DOX, which suggested that

the former one could more efficiently internalize into the cancer cells. The higher cellular uptake of FMPDA/Gd^{3+}/DOX by LM3 cells was also confirmed by flow cytometry (Fig. S9A and S9B). In addition, we also found that P-selectin was upregulated on LM3 cells (Fig. S7). To study the higher cellular uptake was related to P-selectin-mediated endocytosis, LM3 cells were pretreated with P-selectin antibody for 30 min before incubating with FMPDA/Gd^{3+}/DOX. It was found that the internalization of FMPDA/Gd^{3+}/DOX into LM3 cells was significantly reduced after the pretreatment of P-selectin antibody (Fig. 3B and S9), which confirmed that FMPDA/Gd^{3+}/DOX could actively target LM3 cells via the specific binding between fucoidan and overexpressed P-selectin. Moreover, we found that the DOX fluorescent signal inside LM3 cells was increased along with the incubation time, suggesting the time-dependent cellular uptake of FMPDA/Gd^{3+}/DOX. The results also revealed that most intracellular DOX fluorescence was visualized inside the nucleus rather than cytoplasm of the cells after 6 h of incubation, which was possibly due to that the acidic lysosome accelerated the release of DOX from FMPDA/Gd^{3+}/DOX. Furthermore, we found that NIR irradiation could result in a higher cellular uptake of FMPDA/Gd^{3+}/DOX (Fig. 3B and S9). Similar to the other previous findings, the heat generated by NIR light-induced photothermal agent could result in an enhanced cell membrane permeability, thereby increasing the cellular internalization of the nanoparticles [45,46].

To study whether the presence of activated platelets could impact the cellular uptake or not, LM3 cells were pretreated with activated platelets for 30 min before incubation with FMPDA/Gd^{3+}/DOX or MPDA/Gd^{3+}/DOX. As shown in Fig. 3C and S10, the pretreatment of activated platelets could reduce the cellular uptake of MPDA/Gd^{3+}/DOX to some extent. This observation could be explained by the reason that the activated platelets could adhere with the tumor cells, which therefore prevent MPDA/Gd^{3+}/DOX from contacting the tumor cells [47]. However, the internalization of FMPDA/Gd^{3+}/DOX into LM3 cells was obviously enhanced in the presence of activated platelets (Fig. 3C and S10). This phenomenon was possibly associated with that the activated platelets could act as a "bridge" between the LM3 cells and FMPDA/Gd^{3+}/DOX, therefore increasing the internalization of FMPDA/Gd^{3+}/DOX into the tumor cells [48].

3.7. *In vitro cytotoxicity*

The cytotoxicity of FMPDA/Gd^{3+}/DOX towards LM3 cells were analyzed by MTT assay. It was found that free DOX, MPDA/Gd^{3+}/DOX and FMPDA/Gd^{3+}/DOX all could cause a dose-depended cell death by chemotherapy, as reflect by a reduced cell viability observed in an increased DOX dose (Fig. 3D). The half-inhibitory concentration (IC50) of free DOX, FMPDA/Gd^{3+}/DOX and MPDA/Gd^{3+}/DOX was calculated to be 3.01, 4.56 and 8.42 μg/ml, respectively. This result suggested that FMPDA/Gd^{3+}/DOX could more efficiently kill the cancer cells than MPDA/Gd^{3+}/DOX, which was due to that the former one has a stronger tumor-targeted ability. However, it should be also noted that free DOX had a higher anticancer ability than the other two formulations, which was attributed to that free DOX could readily diffuse into and kill the tumor cells.

The chemo-photothermal combination therapy of FMPDA/Gd^{3+}/DOX on LM3 was also studied. As shown in Fig. 3E, the cell viability of FMPDA/Gd^{3+}without NIR irradiation was still above 95% even at the highest concentration of 200 μg/ml, suggesting that FMPDA/Gd^{3+}itself had a good biocompatibility. It was also observed that FMPDA/$Gd^{3+}$with a low concentration of 40 μg/ml could hardly kill the cancer cells under NIR irradiation. The anticancer ability of FMPDA/Gd^{3+}under NIR irradiation was significantly increased by increasing the particle concentration, suggesting that FMPDA/Gd^{3+}had a concentration-dependent PTT efficacy. At a concentration between 40 and 160 μg/ml, the cell viability of the FMPDA/Gd^{3+}/DOX + NIR group was significantly lower than that of FMPDA/Gd^{3+}/DOX or FMPDA/Gd^{3+}+NIR group, which was due to the combined treatment of chemotherapy and PTT. However, the anticancer ability of FMPDA/Gd^{3+}/DOX + NIR, FMPDA/Gd^{3+}/DOX and FMPDA/Gd^{3+}+NIR group was similar at a concentration of 200 μg/ml, because the chemotherapy and PTT alone was enough to kill most of the cancer cells at a high MPDA concentration. The superior anticancer ability of chemo-photothermal combination therapy was also confirmed by the calcein-AM assay, which revealed that FMPDA/Gd^{3+}/DOX+NIR group had the lowest numbers of survived cells among the treatment groups (Fig. 3F).

3.8. *In vivo targeting ability*

To evaluate whether fucoidan modification could render MPDA with the expected tumor-targeted ability *in vivo*, LM3-tumor-bearing mice were intravenously injected with FMPDA/Gd^{3+}/ICG or MPDA/Gd^{3+}/ICG, respectively. *In vivo* whole-body fluorescence imaging of mice revealed that the accumulation of FMPDA/Gd^{3+}/ICG or MPDA/Gd^{3+}/ICG in tumor tissues increased along with the post-injection time (Fig. 4A). However, it should be noted that the fluorescence signal of tumor site treated with FMPDA/Gd^{3+}/ICG was significantly stronger than that of MPDA/Gd^{3+}/ICG at the same post-injection time, which indicated that FMPDA/Gd^{3+}/ICG had a stronger *in vivo* tumor-targeting efficacy than MPDA/Gd^{3+}/ICG. The specific tumor-targeted ability of FMPDA/Gd^{3+}/ICG was further confirmed by the *ex vivo* imaging of tumor tissues harvested at 24 h post-injection, which presented a considerably stronger fluorescence intensity in the FMPDA/Gd^{3+}/ICG group than that of MPDA/Gd^{3+}/ICG group (Fig. 4B and 4C). Moreover, a high accumulation of nanoparticles was also visualized in the liver tissues, which was attributed to the uptake by the reticuloendothelial system [49].

The *ex vivo* fluorescence images of tumor tissues stained with anti-CD41 were firstly captured to investigate whether or not FMPDA/Gd^{3+}/ICG could bind with the activated platelets recruited in the tumor tissues. As shown in Fig. 4D, the fluorescence signal of FMPDA/Gd^{3+}/ICG was well colocalized with that of CD41, which indicated that FMPDA/Gd^{3+}/ICG could effectively bind with platelets, therefore exhibiting an enhanced tumor targeting efficacy via "platelet bridge". Moreover, the collected tumor tissue

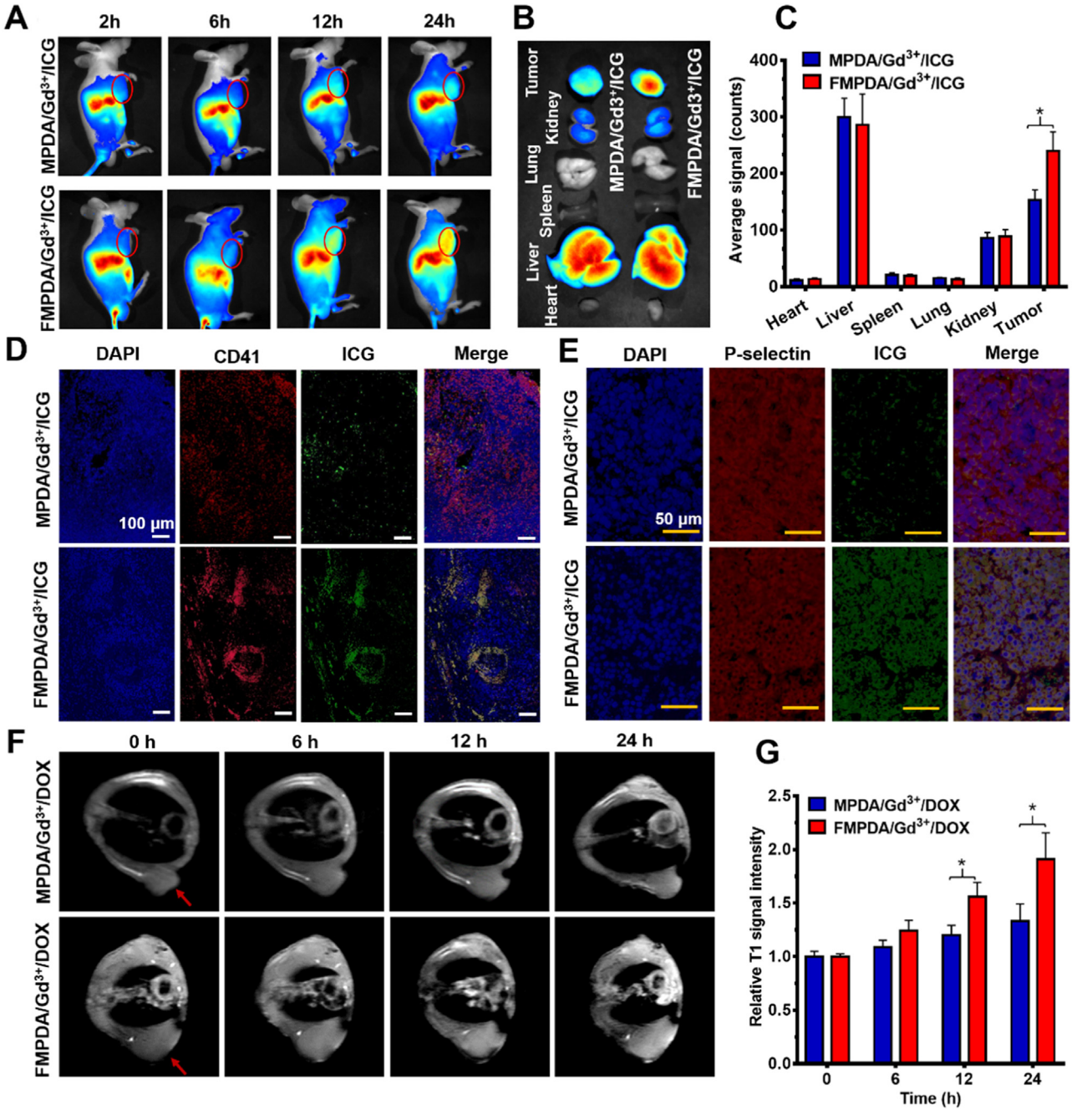

Fig. 4 – *In vivo* targeting ability and MRI performance. (A) *In vivo* biodistribution of MPDA/Gd^{3+}/ICG or FMPDA/Gd^{3+}/ICG in the tumor-bearing mice model, and the marked red circle indicates the tumor site. *Ex vivo* images (B) and the corresponding average signal intensity (C) of the tumor tissue and major organs harvested at 24 h post-injection. (D) Fluorescent images of tumor frozen sections harvested at 24 h post-injection, in which the tumor tissue was stained with DAPI and anti-CD41 antibody, respectively. (E) Fluorescent images of tumor frozen sections harvested at 24 h post-injection, in which the tumor tissue was stained with DAPI and P-selectin antibody, respectively. *In vivo* T1-weighted images (F) and relative T_1 MRI signal intensity (G) of tumors treated before and after treating with MPDA/Gd^{3+}/DOX or FMPDA/Gd^{3+}/DOX. (*$P < 0.05$, $n = 3$).

was stained with anti-CD62P antibody to evaluate the interaction between FMPDA/Gd^{3+}/ICG and P-selectin on the tumor cells. As displayed in Fig. 4E, the fluorescence signals of FMPDA/Gd^{3+}/ICG and P-selectin overexpressed on the tumor cells were overlapped, revealing that FMPDA/Gd^{3+}/ICG could also actively target the tumor cells via P-selectin mediated endocytosis. Thus, we believed that FMPDA/Gd^{3+}/ICG exhibited a superior tumor-targeted capability by simultaneously interacting with the activated platelets and tumor cells with high affinity, which was actually related to the strong P-selectin binding ability.

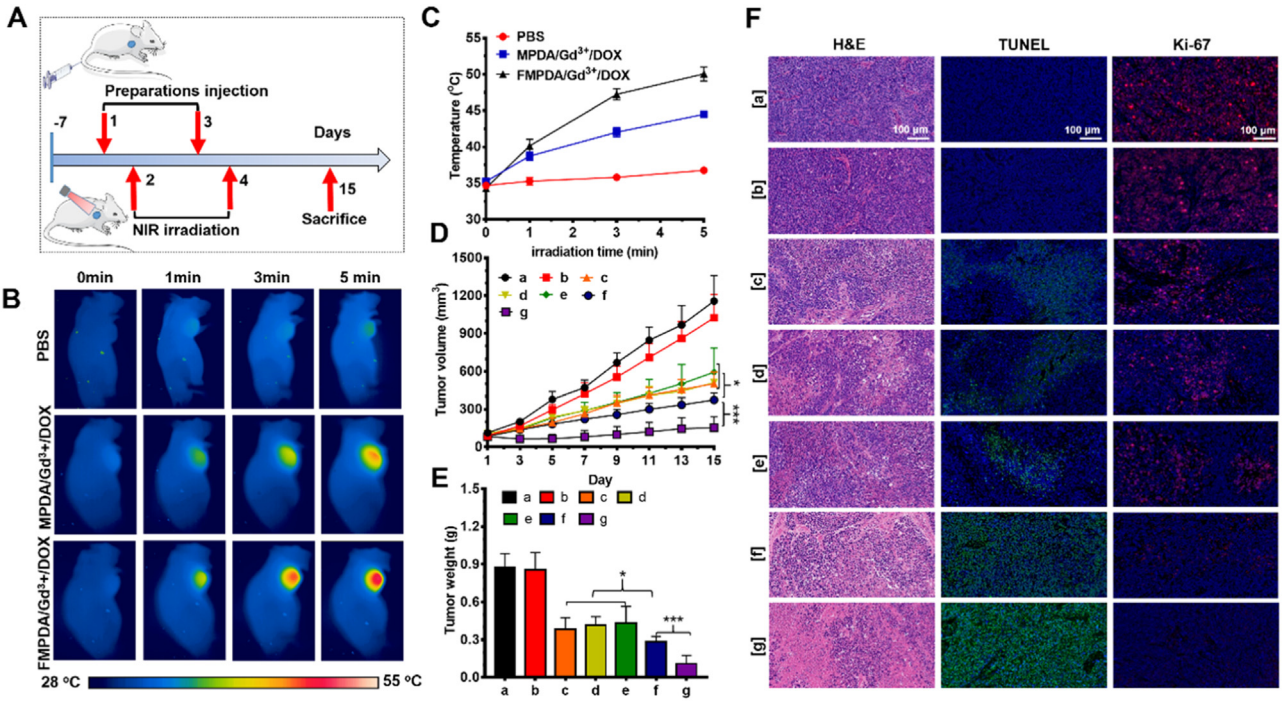

Fig. 5 – *In vivo* anticancer effect. (A) Schematic diagram of the administration method for the therapy. Thermal images (B) and temperature changes (C) of tumors in living mice at 24 h post-injection of FMPDA/Gd^{3+}/DOX, MPDA/Gd^{3+}/DOX or PBS, followed by irradiation with the 808 nm laser (2 W/cm^2) for 5 min. (D) The average tumor growth curves in different groups. (E) The average weight of tumor tissues harvested at Day 15. (F) H&E, tunnel and Ki-67 staining images of tumor tissues in different treatment groups. a, PBS; b, PBS+NIR; c, FMPDA/Gd^{3+}+NIR; d, free DOX; e, MPDA/Gd^{3+}/DOX; f, FMPDA/Gd^{3+}/DOX; g, FMPDA/Gd^{3+}/DOX+NIR. (*$P < 0.05$, *** $P < 0.001$, $n = 5$).

3.9. *In vivo MRI performance*

In this part, *in vivo* MRI performance of FMPDA/Gd^{3+}/DOX was carried out. The tumor-bearing mice were intravenously administrated with FMPDA/Gd^{3+}/DOX or MPDA/Gd^{3+}/DOX, which were then imaged under a 3.0 T MRI scanner at a different pre-set time. As reflected in Fig. 4F, the T_1-weighted MR signals in the tumor region of mice treated with FMPDA/Gd^{3+}/DOX gradually increased against post-injection time. In the case of FMPDA/Gd^{3+}/DOX group, the results also revealed that the T_1-weighted MR signal at 24 h post-injection was almost 2-fold higher than the pre-injected one (Fig. 4G). Moreover, we found that T1-weighted contrast enhancement of FMPDA/Gd^{3+}/DOX groups were more remarkable than that of MPDA/Gd^{3+}/DOX groups (Fig. 4F and 4G). These results could also be explained by the excellent tumor-homing ability of FMPDA/Gd^{3+}/DOX, which led to a higher delivery of contrast agent into the tumor sites. Therefore, *in vitro* and *in vivo* results both indicated that MPDA/Gd^{3+}/DOX could be applied as a promising T_1−MRI contrast agent for cancer diagnosis.

3.10. *In vivo anticancer ability*

In this part, *in vivo* anticancer efficiency of FMPDA/Gd^{3+}/DOX was evaluated, and the treatment protocol was displayed in Fig. 5A. Firstly, we investigated *in vivo* photothermal performance of FMPDA/Gd^{3+}/DOX by monitoring the temperature change of tumor sites during NIR irradiation via an FLIR thermal camera, and PBS and MPDA/Gd^{3+}/DOX were used as controls. As shown in Fig. 5B and 5C, the mice with FMPDA/Gd^{3+}/DOX administration showed a rapid increase of tumor temperature, and it could maintain at about 50 °C during 5 min of NIR irradiation. At the same condition, the tumor temperature of MPDA/Gd^{3+}/DOX and PBS groups was only increased to around 45 °C and 37 °C, respectively. This result demonstrated that FMPDA/Gd^{3+}/DOX had a better *in vivo* photothermal performance than MPDA/Gd^{3+}/DOX, which was attributed to the superior tumor-targeting ability of the former one.

Subsequently, *in vivo* therapeutic effect of different treatment was evaluated. As shown in Fig. 5D and S11, the tumor volume of PBS group was rapidly increased within 15 d Meanwhile, the tumor growth rate of PBS+NIR group was similar to that of PBS group, which indicated that the heat generated by NIR light was not enough to ablate the tumor cells. In comparison, the mice treated with FMPDA/Gd^{3+}showed a significant delay in the tumor growth when combining with NIR irradiation, which could be ascribed to the PTT effect. The tumor inhibition was also observed in free DOX, MPDA/Gd^{3+}/DOX and FMPDA/Gd^{3+}/DOX groups, which was due to the chemotherapy of DOX. Interesting, it was found that the tumor-inhibitory effect of the MPDA/Gd^{3+}/DOX group was not better than the free DOX group. It was well known that MPDA/Gd^{3+}/DOX should release the DOX before

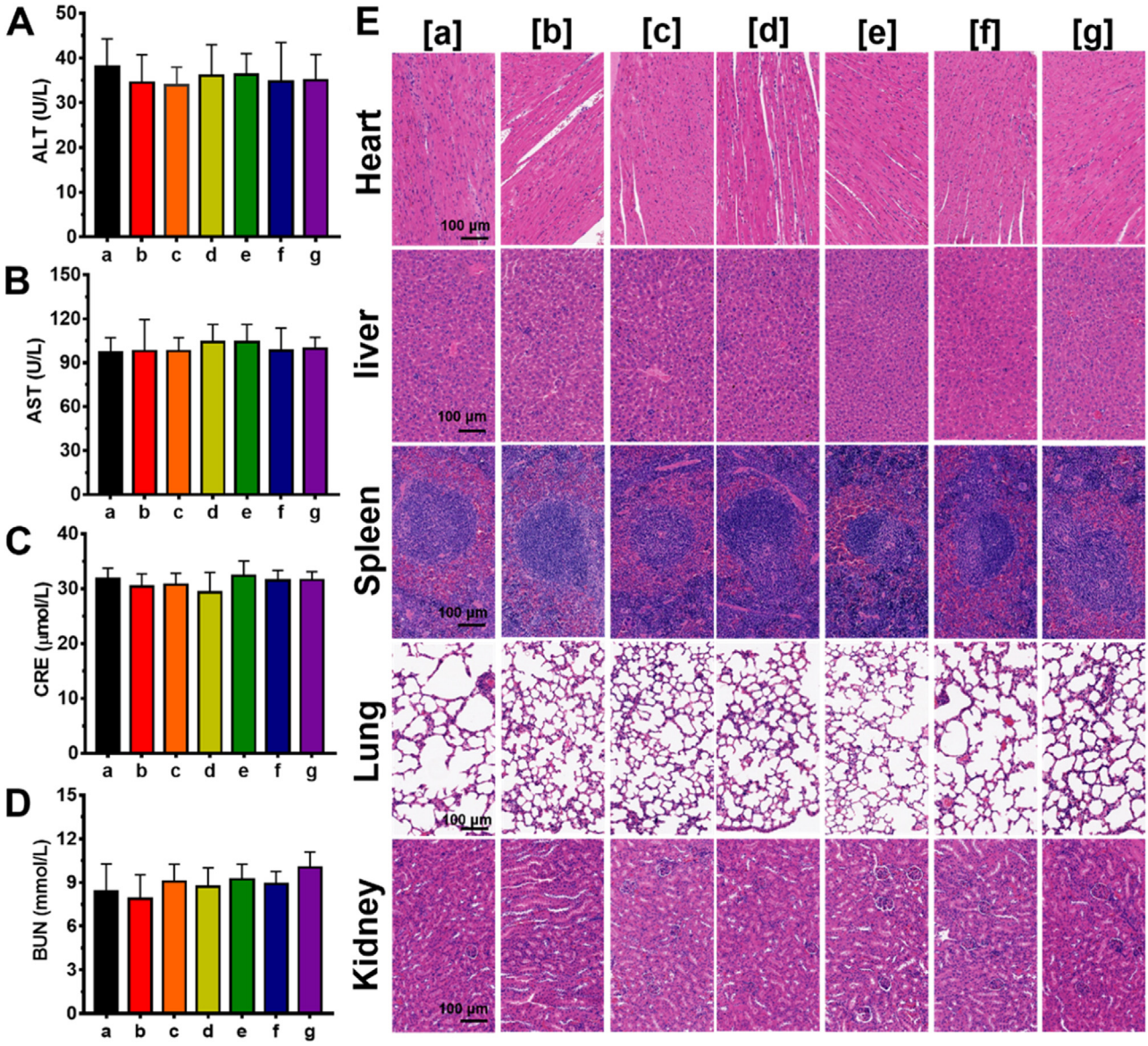

Fig. 6 – Biosafety evaluation. (A-D) Blood biochemistry analysis (AST, ALT, CRE and BUN) of the tumor-bearing mice after various treatments. (E) H&E staining images of the major organs harvested from various groups receiving different treatments. a, PBS; b, PBS+NIR; c, FMPDA/Gd^{3+}+NIR; d, free DOX; e, MPDA/Gd^{3+}/DOX; f, FMPDA/Gd^{3+}/DOX; g, FMPDA/Gd^{3+}/DOX+NIR.

killing the tumor cells. Different from MPDA/Gd^{3+}/DOX, the free DOX could readily diffuse into and kill the cancer cells once they enter into the tumor site. Thus, free DOX had a stronger cytotoxicity than MPDA/Gd^{3+}/DOX, which was also confirmed by MTT assay in our study (Fig. 3D). However, it is well accepted that the nanocarrier could significantly increase the accumulation of free drug (i.e. DOX) into the tumors. Thus, we presumed that the similar tumor-inhibitory effect of the MPDA/Gd^{3+}/DOX and free DOX observed in our study was possibly due to that free DOX had a stronger cytotoxicity but less accumulation in tumor site compared to MPDA/Gd^{3+}/DOX. Some previous studies have also reported that DOX-loaded nanomaterials without tumor-targeted ability do not show a stronger anticancer efficacy than free DOX [50,51]. In comparison, FMPDA/Gd^{3+}/DOX had a stronger anticancer ability than free DOX and MPDA/Gd^{3+}/DOX, which was due to that FMPDA/Gd^{3+}/DOX with a superior tumor-homing ability could largely increase the accumulation of chemotherapeutic drug into the tumor foci. More importantly, the combination treatment of FMPDA/Gd^{3+}/DOX and NIR irradiation could further inhibit the tumor growth, showing the best antitumor capability than the other treatment groups (Fig. 5D and S11). The average weight of tumors collected at the Day 15 showed the same trend with the change of tumor volume (Fig. 5E). These results verified that the chemo-photothermal combination therapy could definitely result in a better therapeutic outcome than the respective single treatment modality.

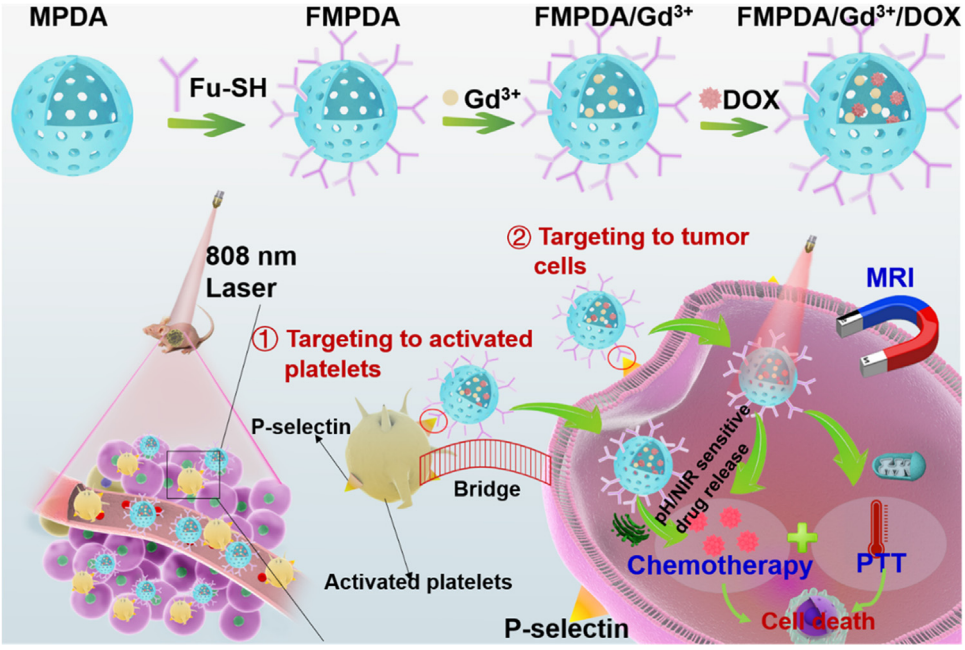

Scheme 1 – In this work, FMDA/Gd^{3+}/DOX was prepared for enhanced cancer theranostics. Due to the specific binding ability between fucoidan and p-selectin, this novel theranostic agent could effectively accumulate into tumor site by simultaneously targeting to the activated paltelets and tumor cells, thereby resulting in an enhanced MRI-guided chemo-photothermal combination therapy of HCC.

To further assess the anticancer effect of different treatment, H&E staining was carried out. As displayed in Fig. 5F, the tumor slices from FMPDA/Gd^{3+}/DOX + NIR groups showed much larger area of cell apoptosis/necrosis regions than the other treatment groups. In accordance with H&E results, the high efficacy of synergistic chemo-photothermal treatment was further confirmed by TUNEL assay, which showed that the numbers of apoptotic cells (green color) in FMPDA/Gd^{3+}/DOX + NIR groups were highest among the treatment groups (Fig. 5F). Moreover, the lowest expression levels of ki67 (proliferative marker) were observed in the tumor sites treated with the combination of FMPDA/Gd^{3+}/DOX and NIR irradiation, indicating that the combined chemo-photothermal treatment could effectively inhibit cancer cell proliferation (Fig. 5F). These results were highly supportive of the best anticancer ability for the tumor-targeted chemo-photothermal combination therapy based on FMPDA/Gd^{3+}/DOX plus NIR irradiation.

3.11. *Biosafety evaluation*

The biological safety is also an important factor for the practice application of a theranostic agent. Hence, the potential adverse effects of FMPDA/Gd^{3+}/DOX were investigated. It was found the tumor-bearing mice treated with free DOX showed some decrease of bodyweight during the initial stage of treatment (Fig. S12), suggesting the toxicity of free DOX. In comparison, the mice treated with FMPDA/Gd^{3+}/DOX were healthy, with their bodyweight remaining steady growth during treatment. Moreover, the biochemistry assays revealed that FMPDA/Gd^{3+}/DOX caused no dysfunction to the liver and kidney, as reflected by the similar levels of biochemistry parameters (ALT, AST, BUN and CRE) between the FMPDA/Gd^{3+}/DOX and normal groups (Fig. 6A-6D). The negligible long-term adverse toxicity of FMPDA/Gd^{3+}/DOX was further confirmed by H&E staining, which showed that FMPDA/Gd^{3+}/DOX did not induce visible damage to the major organs, including heart, liver, spleen, lung, and kidney (Fig. 6E). Overall, these results all verified that FMPDA/Gd^{3+}/DOX could be serve as obvious opportunity for safe cancer theranostics, (Scheme 1).

4. Conclusions

In summary, we successfully fabricated FMPDA/Gd^{3+}/DOX as a novel theranostic agent for MRI-guided chemo-photothermal combination therapy of HCC. The as-prepared FMPDA/Gd^{3+}/DOX had a high photothermal conversion efficiency that could effectively generate heat by converting the adsorbed NIR light. The release of encapsulated DOX from FMPDA/Gd^{3+}/DOX had a dual pH/NIR responsible manner. Moreover, the Gd^{3+} chelation rendered FMPDA/Gd^{3+}/DOX with an excellent T_1–MRI performance, which was conducive to accurate cancer diagnosis. Due to the surface modification of fucoidan, FMPDA/Gd^{3+}/DOX could specifically bind with the p-selectin receptors overexpressed in the tumor-infiltrated platelets as well as the tumor cells, thereby resulting in a higher accumulation in the tumor foci than the one without fucoidan modification. FMPDA/Gd^{3+}/DOX with dual tumor-targeting ability could therefore effectively inhibit the tumor growth under NIR irradiation, which was a result of enhanced

MRI-guided chemo-photothermal combination therapy. Thus, we believed that FMPDA/Gd^{3+}/DOX could provide a new strategy for effective imaging-guided therapy of HCC. On the other hand, the activated platelets also play a vital role in the cancer metastasis. Therefore, it will be meaningful to study the anti-metastatic effect of FMPDA/Gd^{3+}/DOX in future study.

Conflicts of interest

The authors have declared that no competing interest exists.

Acknowledgement

This work was supported by the National Key Research and Development projects intergovernmental cooperation in science and technology of China (2018YFE0126900), National Natural Science Foundation of China (82072025 and 82072026), Zhejiang Provincial Natural Science Foundation (LQ21H180003), Key R&D Program of Lishui City (2021ZDYF12), and Medical Health Science and Technology Project of Zhejiang Provincial Health Commission (2022RC088).

Supplementary materials

Supplementary material associated with this article can be found, in the online version, at doi:10.1016/j.ajps.2022.08.004.

REFERENCES

[1] Sung H, Ferlay J, Siegel RL, Laversanne M, Soerjomataram I, Jemal A, et al. Global cancer statistics 2020: GLOBOCAN estimates of incidence and mortality worldwide for 36 cancers in 185 countries. CA Cancer J Clin 2021;71(3):209–49.
[2] Lammers T, Aime S, Hennink WE, Storm G, Kiessling F. Theranostic nanomedicine. Acc Chem Res 2011;44(10):1029–38.
[3] Wang Y, Shim MS, Levinson NS, Sung HW, Xia Y. Stimuli-responsive materials for controlled release of theranostic agents. Adv Funct Mater 2014;24(27):4206–20.
[4] Ryu JH, Lee S, Son S, Kim SH, Leary JF, Choi K, et al. Theranostic nanoparticles for future personalized medicine. J Control Release 2014;190:477–84.
[5] Ahmed N, Fessi H, Elaissari A. Theranostic applications of nanoparticles in cancer. Drug Discov Today 2012;17(17–18):928–34.
[6] Jain RK, Stylianopoulos T. Delivering nanomedicine to solid tumors. Nat Rev Clin Oncol 2010;7(11):653–64.
[7] Kuang Y, Zhang Y, Zhao Y, Cao Y, Zhang Y, Chong Y, et al. Dual-stimuli-responsive multifunctional Gd2Hf2O7 nanoparticles for MRI-guided combined chemo-/photothermal-/radiotherapy of resistant tumors. ACS Appl Mater Interfaces 2020;12(32):35928–39.
[8] Li Z, Yang Y, Wei H, Shan X, Wang X, Ou M, et al. Charge-reversal biodegradable MSNs for tumor synergetic chemo/photothermal and visualized therapy. J Control Release 2021;338:719–30.
[9] Fernandes N, Rodrigues CF, Moreira AF, Correia IJ. Overview of the application of inorganic nanomaterials in cancer photothermal therapy. Biomater Sci 2020;8(11):2990–3020.
[10] Jiang Z, Li T, Cheng H, Zhang F, Yang X, Wang S, et al. Nanomedicine potentiates mild photothermal therapy for tumor ablation. Asian J Pharm Sci 2021;16(6):738–61.
[11] Zhou Z, Zhang L, Zhang Z, Liu Z. Advances in photosensitizer-related design for photodynamic therapy. Asian J Pharm Sci 2021;16(6):668–86.
[12] Qi J, Xiong Y, Cheng K, Huang Q, Cao J, He F, et al. Heterobifunctional PEG-grafted black phosphorus quantum dots: "Three-in-One" nano-platforms for mitochondria-targeted photothermal cancer therapy. Asian J Pharm Sci 2021;16(2):222–35.
[13] Yan H, Teh C, Sreejith S, Zhu L, Kwok A, Fang W, et al. Functional mesoporous silica nanoparticles for photothermal-controlled drug delivery *in vivo*. Angew Chem Int Ed Engl 2012;51(33):8373–7.
[14] Wang J, Wu X, Shen P, Wang J, Shen Y, Shen Y, et al. Applications of inorganic nanomaterials in photothermal therapy based on combinational cancer treatment. Int J Nanomedicine 2020;15:1903–14.
[15] Lai WF, Wong WT. Use of graphene-based materials as carriers of bioactive agents. Asian J Pharm Sci 2021;16(5):577–88.
[16] Song X, Chen Q, Liu Z. Recent advances in the development of organic photothermal nano-agents. Nano Res 2015;8(2):340–54.
[17] Liu Y, Ai K, Lu L. Polydopamine and its derivative materials: synthesis and promising applications in energy, environmental, and biomedical fields. Chem Rev 2014;114(9):5057–115.
[18] Miao ZH, Wang H, Yang H, Li ZL, Zhen L, Xu CY. Intrinsically Mn^{2+}-chelated polydopamine nanoparticles for simultaneous magnetic resonance imaging and photothermal ablation of cancer cells. ACS Appl Mater Interfaces 2015;7(31):16946–52.
[19] Pu Y, Zhu Y, Qiao Z, Xin N, Chen S, Sun J, et al. A Gd-doped polydopamine (PDA)-based theranostic nanoplatform as a strong MR/PA dual-modal imaging agent for PTT/PDT synergistic therapy. J Mater Chem B 2021;9(7):1846–57.
[20] Hu D, Liu C, Song L, Cui H, Gao G, Liu P, et al. Indocyanine green–loaded polydopamine–iron ions coordination nanoparticles for photoacoustic/magnetic resonance dual-modal imaging-guided cancer photothermal therapy. Nanoscale 2016;8(39):17150–8.
[21] Mu X, Zhang F, Kong C, Zhang H, Zhang W, Ge R, et al. EGFR-targeted delivery of DOX-loaded Fe_3O_4@polydopamine multifunctional nanocomposites for MRI and antitumor chemo-photothermal therapy. Int J Nanomedicine 2017;12:2899–911.
[22] Xing Y, Zhang J, Chen F, Liu J, Cai K. Mesoporous polydopamine nanoparticles with co-delivery function for overcoming multidrug resistance via synergistic chemo-photothermal therapy. Nanoscale 2017;9(25):8781–90.
[23] Zhang L, Yang P, Guo R, Sun J, Xie R, Yang W. Multifunctional mesoporous polydopamine with hydrophobic paclitaxel for photoacoustic imaging-guided chemo-photothermal synergistic therapy. Int J Nanomedicine 2019;14:8647–63.
[24] Wu L, Sun J, Su X, Yu Q, Yu Q, Zhang P. A review about the development of fucoidan in antitumor activity: progress and challenges. Carbohydr Polym 2016;154:96–111.
[25] Ustyuzhanina NE, Bilan MI, Gerbst AG, Ushakova NA, Tsvetkova EA, Dmitrenok AS, et al. Anticoagulant and antithrombotic activities of modified xylofucan sulfate from the brown alga Punctaria plantaginea. Carbohydr Polym 2016;136:826–33.

[26] Fabricius HÅ, Starzonek S, Lange T. The role of platelet cell surface p-selectin for the direct platelet-tumor cell contact during metastasis formation in human tumors. Front Oncol 2021;11:642761.
[27] Shamay Y, Elkabets M, Li H, Shah J, Brook S, Wang F, et al. P-selectin is a nanotherapeutic delivery target in the tumor microenvironment. Sci Transl Med 2016;8(345):345ra87.
[28] Jafari M, Sriram V, Xu Z, Harris GM, Lee JY. Fucoidan-doxorubicin nanoparticles targeting p-selectin for effective breast cancer therapy. Carbohydr Polym 2020;249:116837.
[29] Xu J, Cheng X, Tan L, Fu C, Ahmed M, Tian J, et al. Microwave responsive nanoplatform via P-selectin mediated drug delivery for treatment of hepatocellular carcinoma with distant metastasis. Nano Lett 2019;19(5):2914–27.
[30] Cho MH, Li Y, Lo PC, Lee H, Choi Y. Fucoidan-based theranostic nanogel for enhancing imaging and photodynamic therapy of cancer. Nanomicro Lett 2020;12(1):47.
[31] Chung CH, Lu KY, Lee WC, Hsu WJ, Lee WF, Dai JZ, et al. Fucoidan-based, tumor-activated nanoplatform for overcoming hypoxia and enhancing photodynamic therapy and antitumor immunity. Biomaterials 2020;257:120227.
[32] Li X, Feng Q, Jiang X. Microfluidic synthesis of Gd-based nanoparticles for fast and ultralong MRI signals in the solid tumor. Adv Healthc Mater 2019;8(20):1900672.
[33] Wu H, Hu H, Wan J, Li Y, Wu Y, Tang Y, et al. Hydroxyethyl starch stabilized polydopamine nanoparticles for cancer chemotherapy. Chem Eng J 2018;349:129–45.
[34] Tao B, Yin ZN. Synthesis of HA-SS-MP: a prodrug with high specificity for cancer cells. Nat Prod Commun 2020;15(6):1934578X20932761.
[35] Guan BY, Zhang SL, Lou XW. Realization of walnut-shaped particles with macro-/mesoporous open channels through pore architecture manipulation and their use in electrocatalytic oxygen reduction. Angew Chem Int Ed Engl 2018;57(21):6176–80.
[36] Liu Y, Ai K, Liu J, Deng M, He Y, Lu L. Dopamine-melanin colloidal nanospheres: an efficient near-infrared photothermal therapeutic agent for *in vivo* cancer therapy. Adv Mater 2013;25(9):1353–9.
[37] Zhang Y, Zhu X, Chen X, Chen Q, Zhou W, Guo Q, et al. Activated platelets-targeting micelles with controlled drug release for effective treatment of primary and metastatic triple negative breast cancer. Adv Funct Mater 2019;29(13):1806620.
[38] Park J, Brust TF, Lee HJ, Lee SC, Watts VJ, Yeo Y. Polydopamine-based simple and versatile surface modification of polymeric nano drug carriers. ACS Nano 2014;8(4):3347–56.
[39] Wang Z, Zou Y, Li Y, Cheng Y. Metal-containing polydopamine nanomaterials: catalysis, energy, and theranostics. Small 2020;16(18):1907042.
[40] Guan Q, Guo R, Huang S, Zhang F, Liu J, Wang Z, et al. Mesoporous polydopamine carrying sorafenib and SPIO nanoparticles for MRI-guided ferroptosis cancer therapy. J Control Release 2020;320:392–403.
[41] Shu G, Chen M, Song J, Xu X, Lu C, Du Y, et al. Sialic acid-engineered mesoporous polydopamine nanoparticles loaded with SPIO and Fe^{3+} as a novel theranostic agent for T1/T2 dual-mode MRI-guided combined chemo-photothermal treatment of hepatic cancer. Bioact Mater 2021;6(5):1423–35.
[42] Xu XL, Chen MX, Lou XF, Du Y, Shu G, Qi J, et al. Sialic acid-modified mesoporous polydopamine induces tumor vessel normalization to enhance photodynamic therapy by inhibiting VE-cadherin internalization. Chem Eng J 2021;414:128743.
[43] Mi P, Kokuryo D, Cabral H, Kumagai M, Nomoto T, Aoki I, et al. Hydrothermally synthesized PEGylated calcium phosphate nanoparticles incorporating Gd-DTPA for contrast enhanced MRI diagnosis of solid tumors. J Control Release 2014;174:63–71.
[44] Wang S, Lin J, Wang Z, Zhou Z, Bai R, Lu N, et al. Core–satellite polydopamine–gadolinium-metallofullerene nanotheranostics for multimodal imaging guided combination cancer therapy. Adv Mater 2017;29(35):1701013.
[45] Zhang M, Zhang L, Chen Y, Li L, Su Z, Wang C. Precise synthesis of unique polydopamine/mesoporous calcium phosphate hollow Janus nanoparticles for imaging-guided chemo-photothermal synergistic therapy. Chem Sci 2017;8(12):8067–77.
[46] Tian B, Wang C, Zhang S, Feng L, Liu Z. Photothermally enhanced photodynamic therapy delivered by nano-graphene oxide. ACS Nano 2011;5(9):7000–9.
[47] Guo R, Deng M, He X, Li M, Li J, He P, et al. Fucoidan-functionalized activated platelet-hitchhiking micelles simultaneously track tumor cells and remodel the immunosuppressive microenvironment for efficient metastatic cancer treatment. Acta Pharm Sin B 2022;12(1):467–82.
[48] Zhao W, Li T, Long Y, Guo R, Sheng Q, Lu Z, et al. Self-promoted albumin-based nanoparticles for combination therapy against metastatic breast cancer via a hyperthermia-induced “platelet bridge”. ACS Appl Mater Interfaces 2021;13(22):25701–14.
[49] Li Q, Chen Y, Zhou X, Chen D, Li Y, Yang J, et al. Hyaluronic acid–methotrexate conjugates coated magnetic polydopamine nanoparticles for multimodal imaging-guided multistage targeted chemo-photothermal therapy. Mol Pharm 2018;15(9):4049–62.
[50] Zhou J, Zhou Q, Shu G, Wang X, Lu Y, Chen H, et al. Dual-effect of magnetic resonance imaging reporter gene in diagnosis and treatment of hepatocellular carcinoma. Int J Nanomedicine 2020;15:7235–49.
[51] Zhang NN, Yu RS, Xu M, Chen XY, Chen CM, Xu XL, et al. Visual targeted therapy of hepatic cancer using homing peptide modified calcium phosphate nanoparticles loading doxorubicin guided by T1 weighted MRI. Nanomedicine: NBM 2018;14(7):2167–78.